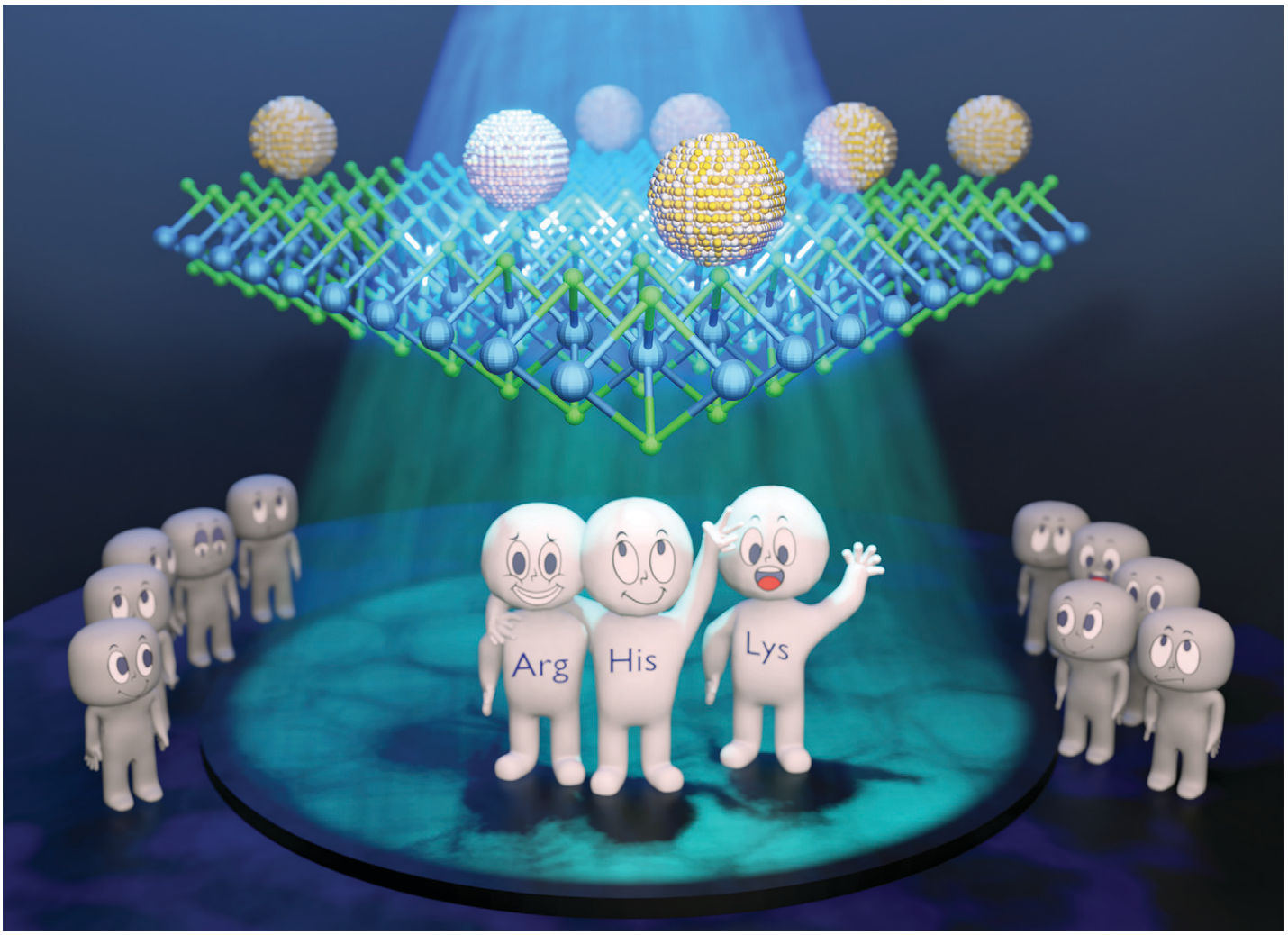

Showcasing research from Professor Jobin Cyriac's laboratory, Department of Chemistry, Indian Institute of Space Science and Technology, Thiruvananthapuram, Kerala, India.

Detection and screening of basic amino acids using the luminescence switching of WS_2 nanosheets–Ag_2O nanoparticles composite

A 0D-2D composite material was prepared by combining WS_2 nanosheets and Ag_2O nanoparticles. The fluorescence from WS_2 nanosheets was quenched in the presence of Ag_2O nanoparticles. The spectral overlap of the nanosheets' emission with surface plasmon resonance absorption of Ag_2O nanoparticles explains the nonradiative energy transfer. The quenched fluorescence was selectively recovered in the presence of three basic amino acids, His, Lys and Arg, at a pH below the isoelectric point of each amino acid.

As featured in:

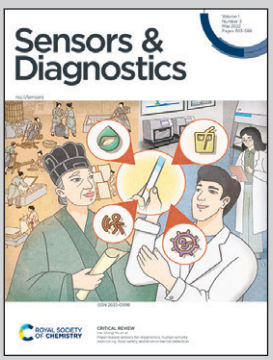

See Jobin Cyriac *et al.*, *Sens. Diagn.*, 2022, **1**, 485.

ROYAL SOCIETY OF CHEMISTRY

rsc.li/sensors

Registered charity number: 207890

Sensors & Diagnostics

PAPER

View Article Online
View Journal | View Issue

Cite this: *Sens. Diagn.*, 2022, **1**, 485

Detection and screening of basic amino acids using the luminescence switching of a WS_2 nanosheet–Ag_2O nanoparticle composite†

Neema Pallikkarathodi Mani,[a] Karthika S. Sunil,[b] Ann Mary Tomy,[a] Bhasha Sathyan[a] and Jobin Cyriac *[a]

The Förster resonance energy transfer (FRET) pair-based detection has gained considerable attention due to its promising sensitivity and selectivity. Herein, we report a turn-on sensor for detecting basic amino acids utilizing the fluorescence emission properties of WS_2 nanosheets (WS_2 NSs). The sensor functions based on a FRET dyad. The addition of $AgNO_3$ into an alkaline solution of WS_2 NSs leads to the *in situ* formation of silver oxide nanoparticles (Ag_2O NPs). The negative surface charge and the presence of sulphur vacancies, together with the possibility for a multiplexed adsorption platform of WS_2 NSs, account for the formation Ag_2O NPs on their surface. In the WS_2 NS–Ag_2O NP system (termed as a 0D–2D composite), the fluorescence emission of the nanosheets became subdued due to the FRET. This 0D–2D composite is proven to be an excellent turn-on sensor for basic amino acids. Histidine, lysine and arginine can induce the aggregation of the Ag_2O NPs, which shuts the FRET pathway, along with the regeneration of the fluorescence of WS_2 NSs. The aggregation of Ag_2O NPs occurs in a sensor solution with pH below the isoelectric points of the amino acids to help to discriminate them. The dynamic range and limit of detection of the sensor have been evaluated. The protein detection capability of the sensor was verified using a lysine containing protein, ubiquitin, and by real sample analysis, using biological fluids.

Received 18th January 2022,
Accepted 9th March 2022

DOI: 10.1039/d2sd00009a

rsc.li/sensors

1. Introduction

One of the salient features of atomically thin, 2D layered materials is the interrelation of their dimensionality and fundamental properties.[1,2] The quantum confinement effect that emerged upon scaling down the dimensions is manifested as photoluminescence (PL) with an improved quantum yield, enabling these materials to be used as fluorescent-based chemical sensors.[3,4] The natural abundance of transition metal dichalcogenides (TMDs) such as MoS_2, WS_2, *etc.*, makes them attractive in the research realm of 2D layered materials. The increased demand in the market for miniaturization of electronic devices and their semiconducting nature with a sizeable bandgap catalyzes such studies. Layered TMDs of formula MX_2 typically have a thickness of 6–9 Å and consist of a single layer of hexagonally packed metal atoms sandwiched between two layers of chalcogen atoms.[5,6] The atoms within the layer are bonded by strong covalent bonds, whereas different layers are held together by weak van der Waals interactions, which enable them to exfoliate into monolayers with the emergence of exotic properties.[7] In layered materials, the van der Waals interactions are not limited to interplanar interactions. Generally, any passivated, dangling bond-free surface interacts with another moiety *via* van der Waals forces. Consequently, any layered 2D material can be integrated with various materials of different dimensionalities to form mixed-dimensional structures. 0D–2D materials are such heterostructures produced by integrating 2D materials with 0D materials, primarily through noncovalent interactions. The 2D components may be graphene or transition metal dichalcogenides (TMDCs) and the 0D components may be small organic molecules or quantum dots (QDs). In contrast to conventional, epitaxially grown heterostructures, the interface in a mixed-dimensional structure is relatively complex and less constrained due to the absence of the need for lattice matching. The usual discontinuity in the band structure and resulting potential energy barriers, the density of states (DOS), also undergoes an abrupt transition, which has several observable implications, such as additional resistance at the junction that results from the change in the number of conductance channels.

Amino acids (AAs), being the building units of proteins, are associated with various physiological processes and are vital

[a] *Department of Chemistry, Indian Institute of Space Science & Technology, Thiruvananthapuram – 695 547, India. E-mail: jobincyriac@iist.ac.in*
[b] *Department of Chemistry, Indian Institute of Science Education and Research, Berhampur – 760010, India*

† Electronic supplementary information (ESI) available. See DOI: 10.1039/d2sd00009a

components of life processes.[8,9] For example, one of the basic amino acids, lysine (Lys), is associated with weight gain in animals, polyamine synthesis and the Krebs–Henseleit cycle.[10] Histidine (His), another basic AA, is closely related to the growth and repair of tissues, the control of transmission of metal elements in biological bases, *etc.*[11] Arginine (Arg), the third and most basic AA, is known for its association with cell division, immune function, the healing of wounds, the release of hormones, *etc.*[12] The AA detection, in general, is thus significant in terms of valuable information it can render in the fields of nutritional analysis and diagnosis of diseases such as Alzheimer's, pancreatitis, *etc.* Among AAs, the detection of thiol-containing AAs is relatively easy owing to their unique nucleophilicity,[13] whereas discrimination of non-thiol-containing AAs is still challenging. Electrochemical and chromatographic approaches are widely used strategies for the detection and characterization of AAs.[14–19] Yet, the demand for sophisticated instruments, operational inconveniences, economic viabilities, choice of various parameters such as response time, detection limit, *etc.*, pave the way for the quest for more desirable and convenient methods. Optical chemosensors are marked with their high sensitivity with notable selectivity along with the possibility of visual discrimination.[8] Hence, a potential fluorometric probe for recognizing specific AAs susceptible to high-throughput assays holds a breakthrough in the current scenario.

Several nanomaterials are demonstrated as signal transducers in colourimetric/fluorescence chemical sensors. The ease of surveilling the light signal has made them a potential candidate in surface plasmon resonance (SPR)-based calorimetric sensing. Many reports that exploit the changes in the SPR peak of noble metal nanoparticles upon interaction with AAs are available. For example, *p*-sulfonatocalix[4]arene thiol modified Au nanoparticles have been used as a colourimetric sensor for His, Lys and Arg in water, based on the principle of broadening and shifting of SPR bands to the red region upon interaction, with linear detection limits of 1 mM, 2 mM and 4 mM, respectively.[20] Chiral detection of L-His was reported based on L-arginine-sulfonated-substituted zinc tetraphenylporphyrin modified Ag nanoparticles (L-Arg–ZnTPPS–Ag NPs).[21] Many groups reported fluorescence-based detection of AAs with improved sensitivity. Lu *et al.* utilized the fluorescence emission of a water-soluble fluorescein-bis-acrylate carrying pyridinium moiety having high sensitivity towards biothiols, which can discriminate simultaneously basic amino acids and thiol-containing amino acids from other amino acids.[13] A simple fluorescent turn-on sensor, employing two complementary cucurbit[*n*]uril microarrays, has been demonstrated for the sensitive detection of basic AAs in water.[22] A close observation of the literature reveals that the detection strategy depends on either the agglomeration of nanoparticles followed by a change in the SPR band or the change in the fluorescence emission of the probe. A combined approach with the ease of agglomeration of nanoparticles and the sensitivity of the fluorescence turn-on methodology would be attractive in chemical sensor applications.

Here, we report a fluorescence sensor for basic amino acids based on WS_2 nanosheet–silver oxide nanoparticle (WS_2 NS–Ag_2O NP) composite materials. The composite was prepared *via* the *in situ* formation of silver oxide nanoparticles (Ag_2O NPs) by the combined action of fluorescent WS_2 nanosheets (WS_2 NSs) in the presence of NaOH. The luminescent WS_2 NSs were synthesized using a facile hydrothermal method. The fluorescence of WS_2 NSs was quenched upon the formation of Ag_2O NPs due to resonance energy transfer. The obvious spectral overlap of WS_2 NS emission with that of surface plasmon resonance (SPR) absorption of Ag_2O NPs explains the nonradiative energy transfer. The quenched fluorescence was selectively recovered in the presence of three basic amino acids: His, Lys and Arg, at a pH below the isoelectric point of each amino acid. The fluorescence recovery was attributed to the aggregation of Ag_2O NPs and thereby the lack of spectral overlap between WS_2 NSs and Ag_2O NPs. The sensor has an appreciable dynamic range and limit of detection (LOD) for all three AA analytes. The formation of Ag_2O NPs, the comprehensive mechanism of quenching and the recovery of fluorescence of WS_2 NSs were proposed with experimental support. The real sample analysis was also demonstrated using biological fluids.

2. Experimental

2.1 Synthesis of WS_2 nanosheets

The WS_2 nanosheets were prepared by hydrothermal reaction of commercially available WS_2 powder and NaOH in an aqueous medium by taking a molar ratio of 1 : 1. Briefly, WS_2 powder (100 mg) was mixed with NaOH (16.0 mg) in 10 mL of water. The resultant solution was taken in a Teflon-lined autoclave and kept for 24 h at 220 °C. The solution after the reaction was centrifuged at 3000 rpm for 30 min; the supernatant was collected, filtered and dialyzed for 3 h using a dialysis bag (molecular weight cut off 500). These purified, light-yellow solutions were used for all further studies.

2.2 Synthesis of the WS_2 nanosheet–Ag_2O NP nanocomposite

To a 2.5 mL of purified WS_2 nanosheet solution, aliquots of $AgNO_3$ solution (1, 2, 3 or 4 mL of 0.02 M) were added dropwise by stirring. The colour of the solution turned yellow *in situ* due to the formation of Ag_2O NPs on the surface of the WS_2 nanosheets.

3. Results and discussion

3.1 Synthesis and characterization of WS_2 nanosheets

In parallel with the steadily growing interest in 2D layered materials, different synthetic strategies have been reported for these materials. We propose a simple approach to prepare 2D layered materials in a nanosize regime employing a hydrothermal reaction. The vigorous reaction of WS_2 powder with a 1 : 1 molar ratio of NaOH at 220 °C yielded exfoliated WS_2 nanosheets. The optimized reaction time for the best

photoluminescence (PL) properties was 24 h. Detailed microscopy and photophysical characterization techniques have been carried out to understand the structural and optical attributes of the material. The transmission electron microscopy (TEM) images (see Fig. 1) show the formation of NSs with a lateral dimension in the range of a few hundreds of nanometers. Notably, the crystallinity of the sheets is maintained even after the vigorous hydrothermal reaction, as evident in the selected area electron diffraction (SAED) pattern. The AFM micrographs confirm the formation of nanosheets with a few layer thicknesses (Fig. S1, ESI†). The thickness measurement from the height profiles drawn at different regions of the AFM micrographs confirms the layer thickness of 2.8 nm, indicating the presence of 2–3 layers of sheets.

Raman spectroscopy can effectively determine the number of layers in the exfoliated TMDs. Generally, there are four major Raman-active modes in bulk WS_2, namely A_{1g}, E_{1g}, E^1_{2g}, and E^2_{2g} modes. Due to the forbidden selection rule in the back-scattering geometry and the limited rejection against Rayleigh scattering, it is challenging to detect the E_{1g} and E^2_{2g} modes, respectively.[23–26] However, the in-plane vibrational E^1_{2g} mode and the out-of-plane vibrational A_{1g} mode are more significant as they can be used to identify the number of layers present in the sheets. A thorough study regarding the frequency trends of the A_{1g} and E_{2g} modes with varying layer thicknesses was performed by Molina-Śanchez and Wirtz.[27] As the number of layers increases from monolayer to bulk, the A_{1g} mode tends to blue-shift, whereas the E^1_{2g} mode shows a red-shift. The weak interlayer interactions and strong dielectric screening of the long-range Coulomb interactions are reasons for this behavior. Therefore, a direct correlation between the frequency difference ($\Delta\omega$) of the E^1_{2g} mode and A_{1g} mode and the sample thickness can be established.[28] In the present case, for WS_2 nanosheets, the value of $\Delta\omega$ is <65 cm^{-1}, which corresponds to monolayer thickness, invariably denoting the exfoliation of the bulk material into nanosheets of a few layers (Fig. 2a).

The crystalline structure and phase of WS_2 NSs were investigated by X-ray diffraction (XRD), using WS_2 powder as a reference (Fig. S2, ESI†). The diffraction peaks of the powder sample were indexed using JCPDS Card No. 08-0237, corresponding to the pure hexagonal (*P*63/*mmc* space group) WS_2 phase. The (002) peak indicates the neat stacking of layers in the powder sample, along with the peaks corresponding to the (004), (100), (101), (102), (103), (006), (105), (106), (110), (008), (112), (107), (114) and (116) planes.[29,30] It can be observed that all the diffraction peaks of WS_2 NSs can be indexed to the hexagonal 2H phase of bulk WS_2, demonstrating the well resolved crystalline structure of WS_2 NSs exfoliated under the hydrothermal conditions. The absence of any additional peak indicates neither any noticeable impurity nor any phase change to the 1T phase during the synthesis. Besides, the weak signal from the (002) plane, compared to the WS_2 powder, denotes the few-layer structure of WS_2 NSs.[31] The chemical state and elemental composition of WS_2 NSs were examined by X-ray photoelectron spectroscopy (XPS) analysis (Fig. S3, ESI†). The high-resolution core-level XPS peaks corresponding to W^{4+} $4f_{7/2}$ and W^{4+} $4f_{5/2}$ were observed at binding energy values of 33.3 and 35.5 eV, respectively, and a small peak at 39.3 eV for W $5p_{3/2}$ indicates the dominance of the (IV) oxidation state for W in WS_2 NSs.[31–33] The absence of peaks corresponding to the 1T phase (in the range of 31.6–32.2 eV)[34] indicates no phase transformation during the hydrothermal synthesis, corroborating the observation in the XRD spectrum. The peaks at 162.0 and 163.2 eV correspond to the S $2p_{3/2}$ and $2p_{1/2}$ orbitals of divalent S, bonded to W^{4+}. The peaks corresponding to the oxidized form of S are present at binding energy values of 168.0 and 169.2 eV, corresponding to S $2p_{3/2}$ and $2p_{1/2}$, respectively. We surmise that, during the hydrothermal reaction, the edge S may be oxidized, leading to the formation of S and O containing functionalities. These functional groups describe the substantial aqueous solubility and phenomenal temporal stability. A single peak in the high-resolution XPS spectrum of oxygen at 531.6 eV indicates the S–O bonds (Fig. S3c, ESI†). The absence of a W^{6+} oxidation state peak and multiple peaks for oxygen in the XPS spectrum depicts that W did not undergo oxidation during the synthesis.

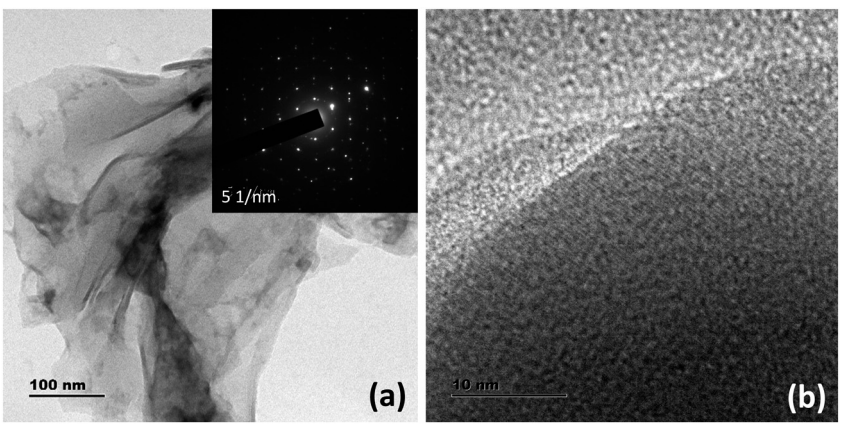

Fig. 1 (a) TEM micrographs of WS_2 nanosheets. The inset of (a) shows the SAED pattern presenting the crystalline nature of the WS_2 nanosheets. (b) Magnified TEM image of the WS_2 NSs depicting the Moiré pattern.

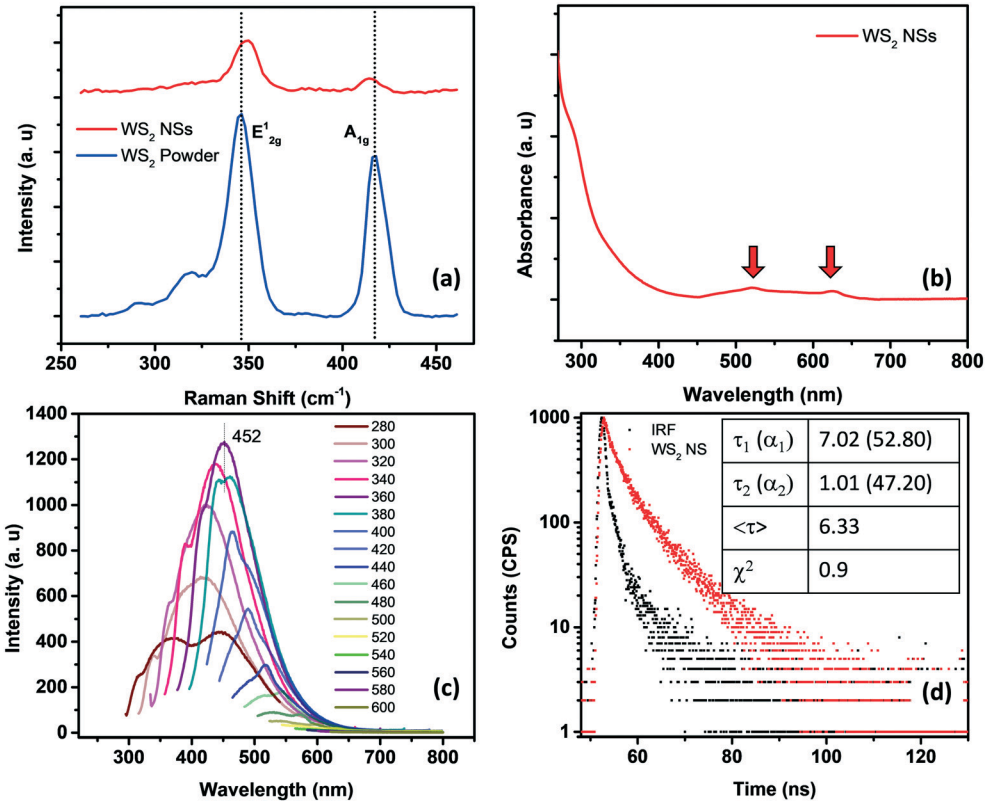

Fig. 2 (a) Raman spectra of WS_2 powder (blue) and WS_2 nanosheets (red). (b) The UV-visible absorption spectrum of WS_2 nanosheets, showing the signature peaks of the sheets corresponding to A and B excitons. (c) Excitation dependent emission spectra of WS_2 NSs. (d) Lifetime spectrum of WS_2 NSs fitted with a bi-exponential function.

The optical signatures of WS_2 NSs have been evaluated using UV-visible and fluorescence spectroscopy. In general, WS_2 powder possesses four major absorption bands at around 630, 528, 456 and 417 nm, which are attributed to A, B, C and D excitons, respectively.[35] The transitions from the spin-splitting valence band to the conduction band at the *K* point of the Brillouin zone are responsible for the emergence of peaks A and B. In contrast, the optical transitions from the deep valence band to the conduction band are denoted as C and D peaks.[36] As the lateral size of the sheets decreases due to enhanced quantum confinement effects and edge effects, these excitonic positions can be blue-shifted.[37] It is known that a continuum of absorption in the excitonic position confirms the phase change of a semiconducting 2H form to a metallic 1T form.[38] The A and B excitons present at 625 and 520 nm, respectively, for WS_2 NSs confirm the retention of the semiconducting nature of the bulk powder after the hydrothermal reaction in the presence of alkali (Fig. 2b). The quantum confinement effects due to the reduction in lateral dimensions of the sheets to the nano regime are manifested as high PL (see the fluorescence spectra given in Fig. 2c). A typical excitation dependent emission was observed for WS_2 NSs, with the best emission centered at 452 nm at an excitation wavelength of 360 nm. The size heterogeneity of the sheets ranging from a few nanometers to micrometers can be one of the reasons behind this behavior. The quantum yield (QY) of the sample calculated using quinine sulphate as a standard has a value of 2.2%, which is comparable with the reported QY value of WS_2 nanosheets.[37,39] Also, the material shows exceptional temporal stability as well as photostability. This remarkable PL from the nanosheets and its inherent stability open the opportunity to exploit these materials in the field of fluorescence-based chemical sensors. Time-resolved fluorescence spectroscopic analysis of WS_2 NSs was performed to unveil the excited state phenomenon occurring within the fluorophore material. The WS_2 NSs are reported to have a very short lifetime of 800 ps.[40] By shrinking the thickness of the bulk materials, the photo-excited carrier lifetime is generally increased due to the enhanced stability of the excitons. In the present case, the decay curves for WS_2 NSs were collected and a bi-exponential fitting was obtained with carrier lifetimes of 2.75 and 9.07 ns by keeping the numerical fitting parameter χ^2 near 1 (Fig. 2d).

3.2 Fabrication of the WS_2 NS-Ag_2O nanoparticle composite

One of the remarkable properties of the present WS_2 NSs is their stable PL for several months under laboratory conditions. It was observed that the PL of the nanosheets was quenched instantaneously by the addition of dil. $AgNO_3$. Upon incremental addition of $AgNO_3$ solution (100 μL each of 0.02 M) to a solution of 2.5 mL of WS_2 nanosheets, at

room temperature, the PL emission is found to plummet accordingly with a change in color of the solution from very light yellow to deep yellow (Fig. 3). The color change, as well as the change in PL, was rapid. This color change was also reflected in the UV-vis spectrum. It has been observed that along with the addition of $AgNO_3$, a new absorption peak below 400 nm emerged (Fig. 3b). The appearance of the yellow color and the new peak at ~400 nm prompted us to surmise that the *in situ* formation of nanoparticles, having surface plasmon resonance (SPR) properties, might have taken place at the surface of WS_2 NSs.

The formation of silver oxide nanoparticles (Ag_2O NPs) from $AgNO_3$ in the presence of NaOH at elevated temperatures is well documented.[41,42] Our WS_2 NS solution contains NaOH, which was left over from the hydrothermal reactions that anticipated the formation of silver oxide nanoparticles. X-ray diffraction studies unveil the nature of the nanoparticles, as the peak positions for silver nanoparticles (which usually form a face centred cubic lattice) will be different from silver oxide nanoparticles (which form cubic crystals upon reaction between $AgNO_3$ and NaOH). The XRD pattern of the WS_2 NS–NP nanocomposite shows remarkable peaks at 2θ values of 27.57°, 31.86°, 38.18°, 46.98°, 54.88°, 64.47° and 69.46°, apart from the peaks corresponding to WS_2 NSs (Fig. S4, ESI†). These peaks were indexed to the (110), (111), (200), (211), (220), (311) and (222) crystal planes of the Ag_2O NPs, having a cubic phase of silver oxide [JCPDS no. 41-1104].[43,44] Therefore, we surmise the formation of Ag_2O NPs. We further carried out XPS analysis to confirm the result obtained from the XRD analysis. The high-resolution XPS spectrum corresponding to Ag 3d shows peaks at 367.5 and 373.5 eV, which can be assigned to $3d_{5/2}$ and $3d_{3/2}$, respectively, of Ag^+ ions in the crystal lattice of Ag_2O (Fig. S5a, ESI†).[43,44] The formation of Ag–O was further confirmed from the XPS spectrum of oxygen 1s. We can observe the emergence of a second peak in the lower energy range of the deconvoluted spectrum of oxygen, corresponding to the Ag–O bond apart from the peak corresponding to the O–S bond (Fig. S5b, ESI†).

Further, TEM analysis confirms the formation of spherical nanoparticles on the surface of WS_2 NSs, forming a typical 0D–2D nanocomposite composed of Ag_2O NPs on the surface of WS_2 NSs (Fig. 4). Optimization of the concentration of WS_2 to $AgNO_3$ was carried out to obtain the homogeneous size distribution of Ag_2O NPs. From TEM, it was evident that, for a volume ratio of 2.5 mL of WS_2 solution, a uniform size distribution of NPs could be seen for 3 mL of 0.02 M $AgNO_3$, and this nanocomposite material is used for further studies. The size distribution of these NPs at various volume ratios along with average diameters is given in Fig. S6.†

One of the significant observations is the quenching of the PL of WS_2 nanosheets upon the formation of the WS_2–Ag_2O NP composite. The general mechanism of quenching involves electron transfer and energy transfer. The spectral overlap of donor emission and acceptor absorption is one of the prerequisites for a celebrated excited-state quenching mechanism, Förster resonance energy transfer (FRET), to materialize. As shown in Fig. 5, there is a remarkable spectral overlap of the absorption of the nanocomposite with the emission of WS_2 NSs. Since the Ag_2O NPs are dispersed on the surface of the nanosheets, the proximity of donor and acceptor species, the second criterion to realize FRET, is satisfied. Therefore, we ascribe the PL quenching to the FRET mechanism because of the presence of Ag_2O NPs with SPR absorption at ~400 nm.

3.3 The nanocomposite as a turn-on sensor for basic amino acids

The quenched fluorescence of WS_2 NSs could be recovered by annihilating the nanosheet–nanoparticle dyad, which opens the possibility of creating a turn-on sensor. We have seen that the quenching occurs in the presence of Ag_2O NPs. Disruption of these Ag_2O NPs can shut the energy transfer

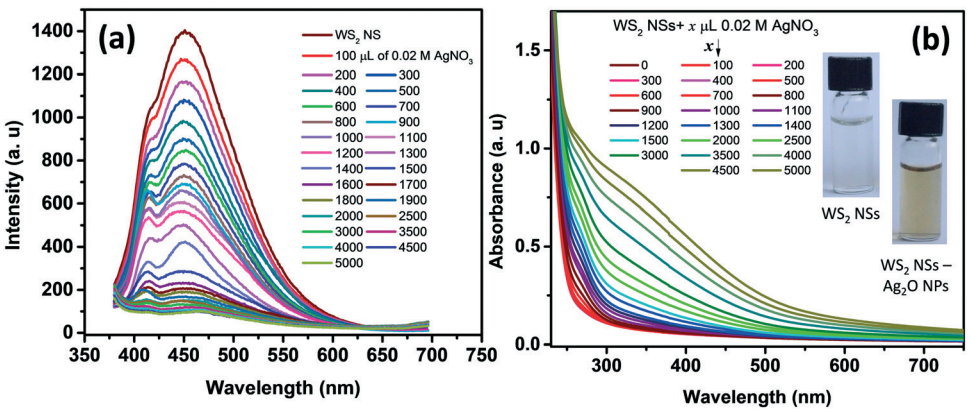

Fig. 3 (a) The PL emission spectra of WS_2 NSs after adding various concentrations of the $AgNO_3$ solution. (b) Absorption spectra of WS_2 nanosheets after adding various concentrations of the $AgNO_3$ solution. The inset of (b) shows the photographs of the WS_2 NS solution and WS_2 NS–Ag_2O NP nanocomposite under visible light.

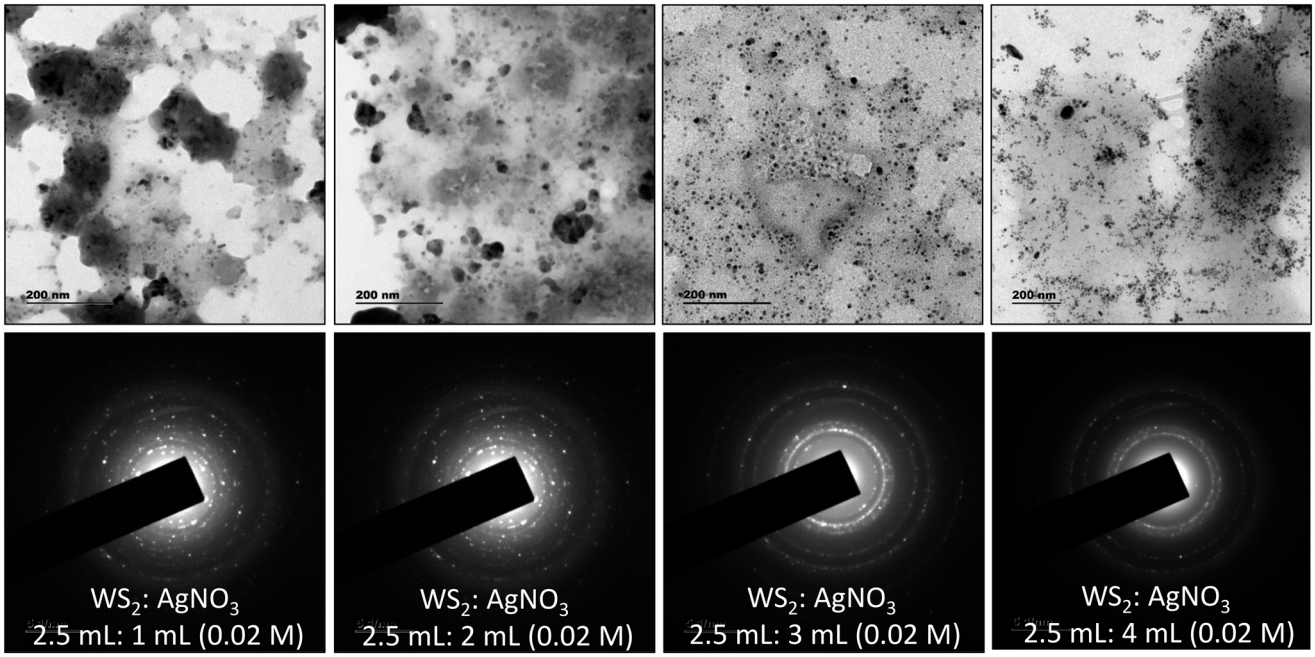

Fig. 4 TEM images and the SAED patterns of WS_2 NSs solution after adding different volumes of $AgNO_3$ solution. The upper pane shows the TEM images and the lower pane shows the SAED patterns. The volume ratio is written in each image.

pathways, and hence, the PL of WS_2 NSs can be recovered. The stability of any colloid is due to the presence of charges on its surface, and in the present case, it can be inferred by zeta potential measurements (Fig. S7, ESI†). Any moiety with a counter charge can destroy the colloidal system and lead to nanoparticle aggregation. Such aggregation of Ag_2O NPs leads to the disappearance of SPR peaks, which is responsible for FRET. The biocompatibility and notable aqueous solubility of Ag_2O NPs and WS_2 NSs prompted us to choose any biologically relevant molecules as analytes. Interestingly, the quenched PL was found to recover with the addition of basic amino acids at a pH value lower than their isoelectric points. We now formulated the WS_2 NS–Ag_2O NP composite material as a turn-on sensor to detect the three basic amino acids His, Lys and Arg.

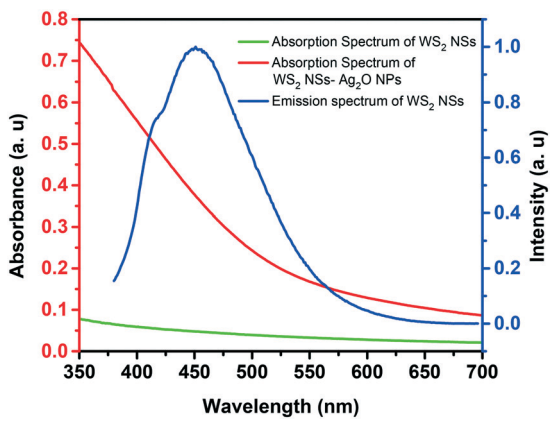

Fig. 5 Spectral overlap of the absorption spectrum of the WS_2 NS–Ag_2O NP composite (red trace) (by the addition of 3.5 mL $AgNO_3$) and the emission spectrum of WS_2 nanosheets (blue trace). The absorption spectrum of WS_2 NSs alone (green) is given for comparison.

3.4 Sensor action

Amino acids, though zwitterionic, tend to be positively charged at a pH below their isoelectric points (p^I).[45] The charges on the surface of AAs can be varied accordingly by changing the pH. The p^I values of His, Lys and Arg are 7.59, 9.74 and 10.76, respectively. Hence at a pH of 7, all three AAs will be positively charged, and at pH 9, Lys and Arg will be positively charged, whereas, at pH 10, only Arg will be positively charged. The PL response of the composite towards the three AAs at pH 7 is given in Fig. 6 and S8, ESI.†

It was noted that the PL responses towards these three AAs (His, Lys and Arg) were distinct from each other. We conducted the experiments at three different pH values: at pH 7, 9 and 10. As evident from Fig. 7, at pH 7, all three AAs could turn-on the PL, whereas the recovery effect is negligible for other AAs and potential interfering biomolecules. Thus, the composite is selective towards the detection of all the basic AAs at pH 7. The selectivity is further evaluated by the selectivity coefficient ($K_{arg} = S_{arg}/S_0$; where S_{arg} is the response of the sensor towards Arg and S_0 is the response of the sensor to other molecules/ions)[46,47] using Arg as the standard at different pH values, and is given in Table S1.† The AA structure with a net positive charge below its isoelectric point provides us room for distinction between the basic AAs (Fig. S9, ESI†). For example, by changing pH 7 to pH 9 or 10, the PL response of the nanocomposite has changed. At pH 9 and 10, His cannot turn on the PL, whereas both Lys and Arg

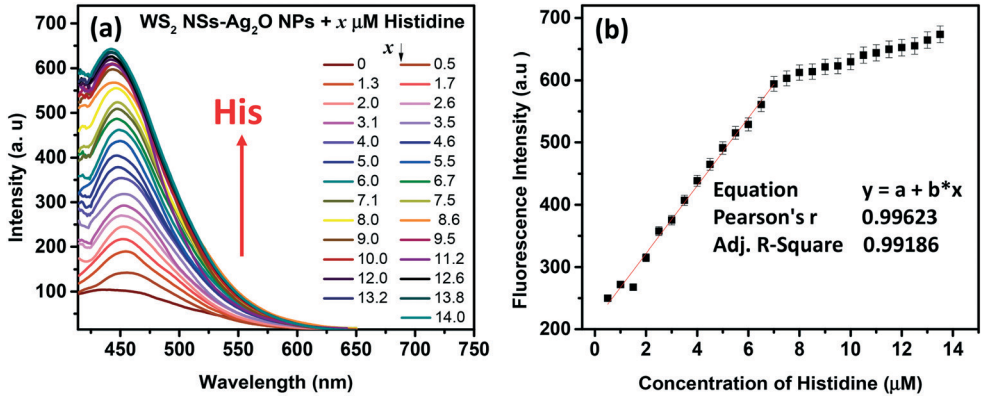

Fig. 6 (a) Response of His towards fluorescence emission of the WS_2 NS–Ag_2O NP nanocomposite at pH 7. The concentration of His in micromolar is given in the figure legend. The excitation wavelength is 360 nm. (b) The calibration curve shows the dynamic range of His. The linear region is considered as the dynamic range of the sensor towards His detection.

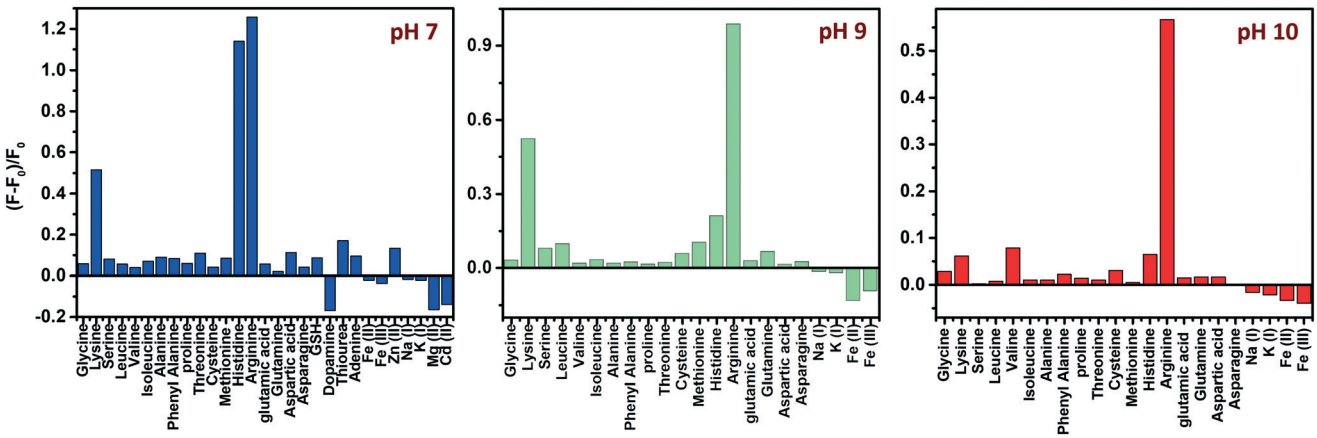

Fig. 7 pH-dependent selectivity: effect of different AAs, other biomolecules and metal ions on the fluorescence intensity of the WS_2 NS–Ag_2O NP nanocomposite at three different pH values.

could still turn-on the emission of the nanocomposite. And at pH 10, Lys also fails to recover the PL of the composite; only Arg can turn-on the emission. Thus, screening within the basic AAs can be accomplished by the 0D–2D nanocomposite sensor solution, merely by altering the pH of the sensor solution. The fluorescence response of the sensor solution towards Lys and Arg at pH 9 and 10, respectively, is given in Fig. S10, ESI.† The dynamic range of His (at pH 7), Lys (at pH 7 and 9) and Arg (at pH 7, 9 and 10) is summarized in Table S2.† The photographs of the WS_2 NSs, WS_2 NS–Ag_2O NP nanocomposite, and nanocomposite solution containing His, Lys and Arg under visible and UV light show the possibility of a visual screening (Fig. S11, ESI†). The zeta potential values of the WS_2 NS–Ag_2O NP nanocomposite at various pH values are given in Table S3,† exhibiting its stability at various pH values.

3.5 Mechanism of formation of Ag_2O NPs and fluorescence turn-on sensing

$AgNO_3$ in the presence of NaOH is known to form Ag_2O according to the equation given below.[41] Thus we propose that in the presence of NaOH, which was used for the hydrothermal reaction, Ag_2O particles might have formed.

$$AgNO_3 + NaOH \rightarrow AgOH + NaNO_3$$

$$2AgOH \rightarrow Ag_2O + H_2O$$

The survey scan XPS spectra of WS_2 NSs and the WS_2 NS–Ag_2O NP composite show peaks corresponding to W, S, and O, along with the peaks of Ag in the case of the composite (Fig. 8a and b). The deconvoluted spectra of W of the WS_2 NS–Ag_2O NP composite show peaks corresponding to W $4f_{7/2}$, $4f_{5/2}$ and W $5p_{3/2}$ at slightly lower binding energy values (33.23, 35.33 and 39.13 eV, respectively) comparable to WS_2 NSs, due to the weaker W–S bond (Fig. 8c). These had binding energy values of 33.3, 35.5 and 39.3 eV for the case of WS_2 NSs (see Fig. S3, ESI† and the discussion in section 3.1). The high-resolution XPS peak corresponding to S indicates the chemical reaction possibilities at the nanosheet surface. In both cases, *viz.* NSs alone and the 0D–2D composite, the XPS peak split to W–S and S–O bonds (Fig. 8d and S3†). The peaks assigned to the metal–S bond (162.0 and

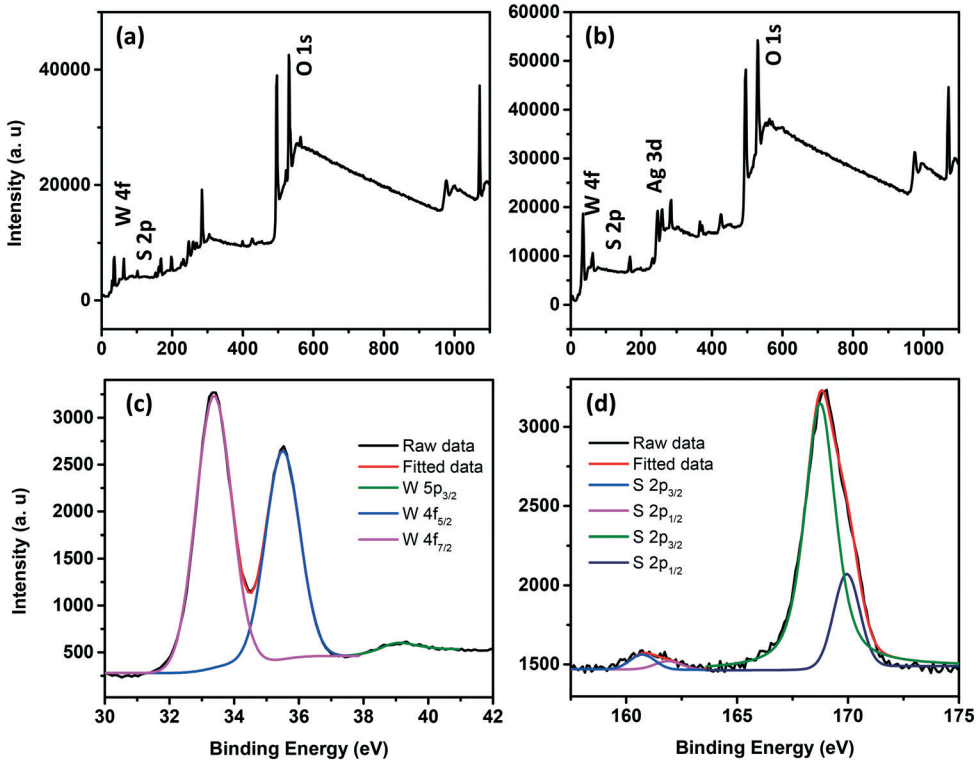

Fig. 8 Survey scan XPS spectra of WS_2 NSs (a) and the WS_2 NS–Ag_2O NP nanocomposite (b). High resolution XPS spectra of the W (c) and S (d) regions of the WS_2 NS–Ag_2O NP nanocomposite.

163.2 eV) for the case of WS_2 NSs have shifted to 160.7 eV and 161.9 eV in the composite material. This peak shift is attributed to the contribution from the Ag–S bond and subsequent peak broadening.

The crucial part of the turn-on sensing mechanism, on the other hand, was mainly determined by the protonated form of the basic AAs below their p^I. In the presence of AAs, the negative charges on the surface of Ag_2O NPs are getting nullified, leading to the aggregation of Ag_2O NPs and hence the reduction of the SPR peak intensity. This decrease in SPR absorption leads to the shutting off of the FRET pathway and the PL is subsequently recovered. The TEM micrographs, UV-visible absorption studies and lifetime analysis corroborate with these assumptions. As shown in the TEM images given in Fig. 9 and S12, ESI,† His, Lys and Arg induce the aggregation of Ag_2O NPs at pH 7. At pH 9, the intact Ag_2O NPs are visible in the nanocomposite samples after adding His. At pH 10, addition of His or Lys does not lead to aggregation. This observation further authenticates the involvement of aggregation for the PL recovery (Fig. S13 and S14, ESI†). The absence of SPR peaks in the in the UV-visible absorption spectra (Fig. S15, ESI†) validates the argument.

Another vital observation of the interaction of AAs with the nanocomposite is the precipitation of Ag_2O NPs upon the

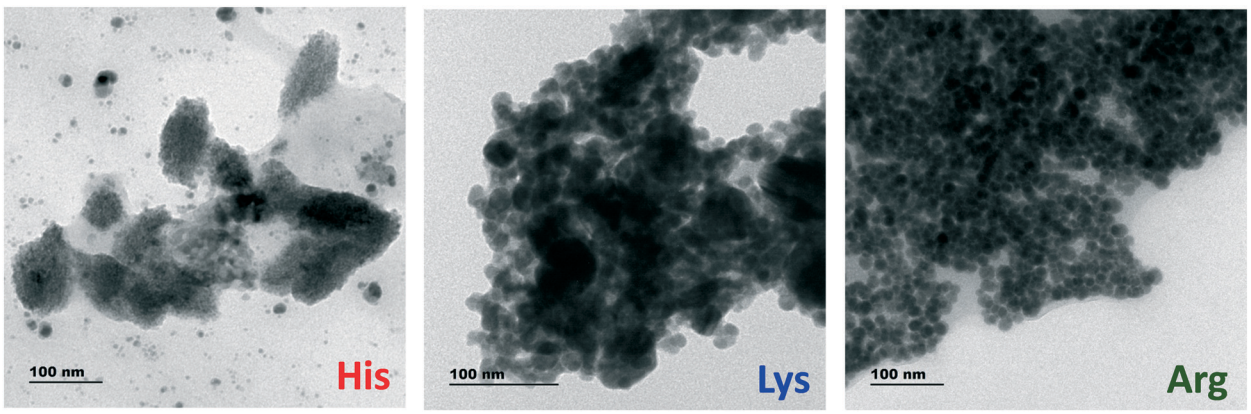

Fig. 9 TEM images of the WS_2 NS–Ag_2O NP nanocomposite upon interaction with His, Lys and Arg at pH 7.

addition of excess AAs (concentration well above the dynamic range). The yellow color of the solution disappeared with the precipitation of Ag_2O as a brown precipitate. The TEM analysis of this colorless supernatant solution shows that Ag_2O NPs have been completely precipitated along with some WS_2 NSs and the solution contains only the remaining WS_2 NSs (Fig. S16, ESI†). The crystallinity and the neat morphology of the sheets were lost after the precipitation of Ag_2O NPs. We surmise that the locations with inscribed markings (in Fig. S16, ESI†) are the spots where the Ag_2O NPs adsorbed onto the nanosheets. The Ag_2O NPs are formed onto the surface of WS_2 NSs and may be stabilized by the groups containing S and O. Also, the dangling S atoms of the nanosheets take part in the reaction, eventually forming compounds like Ag_2S as well. When the NPs detach from the sheets by aggregation followed by precipitation, the remaining sheets contain several etched areas due to the removal of adsorbed Ag_2O NPs along with dangling S groups (as Ag_2S). The etched regions are primarily defects due to S or its functional group vacancies. High-resolution XPS of the supernatant solution shows weak S peaks, which are proof of the removal of S from the sensor material by precipitation of nanoparticles. The oxygen region of the XPS spectrum, nonetheless, shows a single peak at 531.5 eV, as in the case of WS_2 NSs, which invariably shows the S–O bond. The high-resolution XPS analysis of W indicates no significant peak shift from the nanocomposite values (33.22, 35.32, and 39.02 eV), implying that the oxidation state of W was not affected (Fig. S17, ESI†). The absence of peaks corresponding to W–O and the W^{6+} state indicate that the dangling bonds created by the removal of S was not satisfied by oxygen. Notably, a full recovery of PL was not attained even after the addition of AAs well above the dynamic range. This could be attributed to the defects created during the removal of Ag_2O NPs by the precipitation, which can act as seats for nonradiative transfers (Fig. S18, ESI†).

The excited-state lifetime analysis depicts the complexity of the interactions between the AAs and the nanocomposite (Fig. S19, ESI†). It has been observed that, upon the addition of $AgNO_3$ into WS_2 NSs, one of the lifetime components becomes nonradiative with the highest contribution (0.13 ns and 80.38% contribution). We attribute this shift to the energy transfer from WS_2 NSs to Ag_2O NPs formed on their surface. The absence of FRET upon the addition of AAs is substantiated by the recovery of their lifetime values near that of bare/free WS_2 NSs. The emergence of a third lifetime component with a nonradiative pathway for the solutions with His, Lys and Arg might have arisen from the defect created in the sheets during the Ag_2O NP formation.

We were interested in knowing whether the aggregation of Ag_2O nanoparticles (in the WS_2 NS–Ag_2O NP nanocomposite) by basic AAs can be modulated by changing the pH and the fluorescence can be quenched reversibly or not. Interestingly, we observed that the increase in the pH of the sensor solution from 7 to 9 for the analyte His led to the fluorescence quenching. This observation is attributed to the separation of aggregated particles due to increased pH (above the isoelectric value of His). We examined the resultant solution using the UV-visible absorption spectra and TEM (see Fig. S20†). After the pH increase, the WS_2 NS–Ag_2O NP composite shows the presence of a SPR peak at 360 nm, depicting separated Ag_2O NPs. The re-appearance of colour was also observed (see the photographs given in Fig. S20†). The same experiment was done for the analyte Lys at pH 7 and 9 and then the pH was increased to 10. Similar results were obtained. These experiments show that the sensor action is reversible and can be modulated by changing the pH.

3.6 Protein sensing and real sample detection

Protein-specific detection is of fundamental importance for diagnosing and detecting protein biomarkers and deciphering biological processes at cellular levels. Most fluorescent probes work under the principle of changes in their photophysical characteristics upon interaction with the protein through chemical reactions or mere physical interactions. Yet, the fluorescence labelling and subsequent detection are invariably laborious, and the development of a mix-and-detect strategy that employs turn-on-based fluorescence detection will be highly appealing.

To test our fluorescent probe for protein detection, ubiquitin, a regulatory protein found in eukaryotes tissues, was selected as a target protein, as it contains seven lysine residues in its structure. Two significant functions of ubiquitin are marking proteins to be eliminated from the system and modulating the functions of the substrate protein with which it can conjugate without metabolically destabilizing this acceptor protein.[48] The abnormal concentration of ubiquitin is associated with many physiological aberrations. For example, high ubiquitin levels can be observed in the cerebrospinal fluid of Alzheimer's disease patients.[49] Therefore, facile detection and precise quantification of ubiquitin are of utmost importance.

We demonstrated a label-free detection of ubiquitin using the present fluorescent probe, the WS_2 NS–Ag_2O NP composite. The PL intensity is found to be enhanced (6.5 fold) with the ubiquitin concentration from 0 to 61 μg mL^{-1} linearly (R^2 = 0.99) at room temperature without any waiting period (Fig. S21, ESI†). From the UV-vis absorption, the SPR peak of Ag NPs was decreased, suggesting a similar mechanism as we have observed in the case of basic AAs (Fig. S22, ESI†). The lifetime analysis further corroborates these results. As is evident from Fig. S23, ESI,† the lifetime components of WS_2 NSs were regenerated in the presence of ubiquitin with similar contributions [9.1 ns (54.4) and 2.8 ns (45.6) for WS_2 NSs and 8.5 ns (56.4) and 2.3 ns (43.6) for the WS_2 NS–Ag_2O NP nanocomposite with ubiquitin]. The zeta potential values of the WS_2 NS–Ag_2O NP nanocomposite with ubiquitin are also commensurate with the value of WS_2 NSs (Table S3, ESI†). The excitation spectrum (Fig. S24, ESI†) of WS_2 NSs at an emission position of 450 nm shows two peaks at *ca.* 265 and 360 nm, referring to two electronic states

Table 1 The recovery and relative standard deviation of the measurements obtained from real sample analysis

Sample	Spiked (μM)	Observed (mean; μM)	Recovery %	% RSD
Blood sample	1.5	1.5188 ± 0.044	101.25	1.67
	2	2.0038 ± 0.027	100.19	0.81
	2.5	2.5037 ± 0.019	100.15	0.97
Urine sample	1.75	1.7716 ± 0.072	101.24	1.75
	2	2.0031 ± 0.093	100.16	2.03
	2.25	2.2772 ± 0.108	101.21	2.14
	2.5	2.5232 ± 0.092	100.93	1.66

available for the system. The WS_2 NS–Ag_2O NP nanocomposite, on the other hand, has only one major peak at around 310 nm. The disappearance of the longer wavelength peak is attributed to the effective energy transfer due to changes in surface states. However, the re-appearance of the longer wavelength excitation peak (~360 nm) in the case of the WS_2 NS–Ag_2O NP nanocomposite with ubiquitin at 360 nm verifies the shutting off of FRET between WS_2 NSs and Ag_2O NPs in the presence of protein and the regeneration of the fluorescence intensity. The mass spectra of pure protein and protein in the presence of the WS_2 NS–Ag_2O NP composite are given in Fig. S25a and b, ESI.† The characteristic protein peaks are evident in the mass spectrum of pure protein. In contrast, these peaks are absent in the case of the analyte-containing sensor solution (ubiquitin + WS2 NS–Ag2O NP solution) (see Fig. S25a, ESI†). This implies that the protein was bound to the Ag_2O NPs and did not appear in the mass spectrum.

Evaluation of the WS_2 NS–Ag_2O NP nanocomposite utility as a sensor for basic AAs in real sample detection was also performed using blood and urine samples. Detection and quantification of Lys are significant, as they give a straightforward diagnosis of various disorders and diseases with the presence of Lys in urine and plasma.[50] We chose Lys as our analyte for real sample analysis. The samples were prepared by spiking known concentrations of Lys and the fluorescence spectra were recorded after addition to the WS_2 NS–Ag_2O NP nanocomposite at room temperature in buffer solutions. The results obtained are shown in Table 1. The recovery and relative standard deviation of the measurements (% RSD) were evaluated to check the reliability of the present sensor. For both the blood sample and the urine sample, excellent recovery within 2% RSD was obtained, which is superior to those of already reported methods.[51–53] The result indicates the reliability of the sensor for analytical applications.

4. Conclusion

In the present study, we demonstrated a luminescent 2D material, exfoliated WS_2 nanosheets, for sensing biologically relevant molecules. Highly fluorescent and stable WS_2 nanosheets were synthesized using a facile hydrothermal synthetic route. Interestingly, Ag_2O NPs were formed on the WS_2 nanosheets instantaneously by the addition of the $AgNO_3$ solution. The formation of Ag_2O NPs leads to the reduction of PL from WS_2 NSs *via* FRET. We investigated the effect of positively charged basic nanoparticles on the PL of the WS_2 NS–Ag_2O NP composite and fabricated a turn-on sensor for three basic amino acids *viz.* His, Lys and Arg. The easy, straightforward synthetic method for the formation of stable and highly fluorescent WS_2 NSs without using any hazardous solvents, the *in situ* formation of stable Ag_2O NPs without an extra stabilizing agent, and devising a simple aggregation strategy to shut the FRET pathway, thereby ensuring a turn-on detection and screening of all the basic amino acids, are the highlights of the present sensor system. The practical application of the sensor was demonstrated for the detection of protein: ubiquitin and Lys from real samples – blood and urine.

Live subject statement

All experiments were performed in accordance with the guidelines "National ethical guidelines for biomedical and health research involving human participants, Indian Council for Medical Research (ICMR), Government of India", and approved by the ethics committee at "Institutional Ethics Committee (IEC), Indian Institute of Space Science and Technology, Thiruvananthapuram". Informed consents were obtained from the human participants of this study.

Conflicts of interest

There are no conflicts to declare.

Acknowledgements

The authors acknowledge IIST Thiruvananthapuram for funding and the PSG Institute of Advanced Studies, Coimbatore and The National Institute for Interdisciplinary Science and Technology, Thiruvananthapuram for analysis.

References

1 X. Gu, B. Li and R. Yang, *J. Appl. Phys.*, 2016, **119**, 085106.
2 M.-W. Lin, I. I. Kravchenko, J. Fowlkes, X. Li, A. A. Puretzky, C. M. Rouleau, D. B. Geohegan and K. Xiao, *Nanotechnology*, 2016, **27**, 165203.
3 G. Eda, H. Yamaguchi, D. Voiry, T. Fujita, M. Chen and M. Chhowalla, *Nano Lett.*, 2011, **11**, 5111–5116.
4 P. Neema, A. M. Tomy and J. Cyriac, *TrAC, Trends Anal. Chem.*, 2020, **124**, 115797.
5 D. Jariwala, V. K. Sangwan, L. J. Lauhon, T. J. Marks and M. C. Hersam, *ACS Nano*, 2014, **8**, 1102–1120.
6 Q. H. Wang, K. Kalantar-Zadeh, A. Kis, J. N. Coleman and M. S. Strano, *Nat. Nanotechnol.*, 2012, **7**, 699–712.
7 A. Splendiani, L. Sun, Y. Zhang, T. Li, J. Kim, C. Chim, G. Galli and F. Wang, *Nano Lett.*, 2010, **10**, 1271–1275.
8 Y. Zhou and J. Yoon, *Chem. Soc. Rev.*, 2012, **41**, 52–67.
9 S. S. Sharma and K.-J. Dietz, *J. Exp. Bot.*, 2006, **57**, 711–726.
10 H. Yoshida, Y. Nakano, K. Koiso, H. Nohta, J. Ishida and M. Yamaguchi, *Anal. Sci.*, 2001, **17**, 107–112.

11 D. Xiong, M. Chen and H. Li, *Chem. Commun.*, 2008, 880–882.
12 T. Liu, N. Li, J. X. Dong, Y. Zhang, Y. Z. Fan, S. M. Lin, H. Q. Luo and N. B. Li, *Biosens. Bioelectron.*, 2017, **87**, 772–778.
13 X. Lu, W. Wang, Q. Dong, X. Bao, X. Lin, W. Zhang, X. Dong and W. Zhao, *Chem. Commun.*, 2015, **51**, 1498–1501.
14 S. T. R. Naqvi, T. Rasheed, M. N. Ashiq, M. N. ul Haq, S. Majeed, B. Fatima, R. Nawaz, D. Hussain and S. Shafi, *Polyhedron*, 2020, 114426.
15 H. Liu, J. Shao, L. Shi, W. Ke, F. Zheng and Y. Zhao, *Sens. Actuators, B*, 2020, **304**, 127333.
16 E. V. Suprun, E. V. Karpova, S. P. Radko and A. A. Karyakin, *Electrochim. Acta*, 2020, **331**, 135289.
17 M. Hasanzadeh, A. Karimzadeh, N. Shadjou, A. Mokhtarzadeh, L. Bageri, S. Sadeghi and S. Mahboob, *Mater. Sci. Eng., C*, 2016, **68**, 814–830.
18 J. L. da Silva, M. A. Beluomini, G. C. Sedenho and N. R. Stradiotto, *Microchem. J.*, 2017, **134**, 374–382.
19 B. R. Kolanu, V. Boddula, S. Vadakedath and V. Kandi, *Cureus*, 2017, **9**(3), e1091.
20 G. Patel and S. Menon, *Chem. Commun.*, 2009, 3563–3565.
21 Y. Sun, L. Zhang and H. Li, *New J. Chem.*, 2012, **36**, 1442–1444.
22 T. Minami, N. A. Esipenko, B. Zhang, L. Isaacs and P. Anzenbacher, *Chem. Commun.*, 2014, **50**, 61–63.
23 H. Zeng, G.-B. Liu, J. Dai, Y. Yan, B. Zhu, R. He, L. Xie, S. Xu, X. Chen and W. Yao, *Sci. Rep.*, 2013, **3**, 1–5.
24 X. Zhang, X.-F. Qiao, W. Shi, J.-B. Wu, D.-S. Jiang and P.-H. Tan, *Chem. Soc. Rev.*, 2015, **44**, 2757–2785.
25 Y. Zhao, X. Luo, H. Li, J. Zhang, P. T. Araujo, C. K. Gan, J. Wu, H. Zhang, S. Y. Quek and M. S. Dresselhaus, *Nano Lett.*, 2013, **13**, 1007–1015.
26 H. Li, J. Wu, Z. Yin and H. Zhang, *Acc. Chem. Res.*, 2014, **47**, 1067–1075.
27 A. Molina-Sanchez and L. Wirtz, *Phys. Rev. B*, 2011, **84**, 155413.
28 H. Zeng, G.-B. Liu, J. Dai, Y. Yan, B. Zhu, R. He, L. Xie, S. Xu, X. Chen and W. Yao, *Sci. Rep.*, 2013, **3**, 1608.
29 Y. Cheng, J. Peng, B. Xu, H. Yang, Z. Luo, H. Xu, Z. Cai and J. Weng, *IEEE Photonics J.*, 2016, **8**, 1.
30 X. Zhang, W. Lei, X. Ye, C. Wang, B. Lin, H. Tang and C. Li, *Mater. Lett.*, 2015, **159**, 399–402.
31 G.-Q. Han, Y.-R. Liu, W.-H. Hu, B. Dong, X. Li, Y.-M. Chai, Y.-Q. Liu and C.-G. Liu, *Mater. Chem. Phys.*, 2015, **167**, 271–277.
32 K. Zhang, L. Fu, W. Zhang, H. Pan, Y. Sun, C. Ge, Y. Du and N. Tang, *ACS Omega*, 2018, **3**, 12188–12194.
33 X. Mao, Y. Xu, Q. Xue, W. Wang and D. Gao, *Nanoscale Res. Lett.*, 2013, **8**, 430.
34 S. X. Leong, C. C. Mayorga-Martinez, X. Chia, J. Luxa, Z. Sofer and M. Pumera, *ACS Appl. Mater. Interfaces*, 2017, **9**, 26350–26356.
35 A. Bayat and E. Saievar-Iranizad, *J. Lumin.*, 2017, **185**, 236–240.
36 A. K. Mishra, K. V. Lakshmi and L. Huang, *Sci. Rep.*, 2015, **5**, 15718.
37 W. Zhao, Z. Ghorannevis, L. Chu, M. Toh, C. Kloc, P.-H. Tan and G. Eda, *ACS Nano*, 2013, **7**, 791–797.
38 B. Mahler, V. Hoepfner, K. Liao and G. A. Ozin, *J. Am. Chem. Soc.*, 2014, **136**, 14121–14127.
39 B. Zhu, X. Chen and X. Cui, *Sci. Rep.*, 2015, **5**, 9218.
40 L. Yuan and L. Huang, *Nanoscale*, 2015, **7**, 7402–7408.
41 K. T. Sullivan, C. Wu, N. W. Piekiel, K. Gaskell and M. R. Zachariah, *Combust. Flame*, 2013, **160**, 438–446.
42 M. Padilla Villavicencio, A. Escobedo Morales, M. Ruiz Peralta, M. Sánchez-Cantú, L. Rojas Blanco, E. Chigo Anota, J. H. Camacho Garcia and F. Tzompantzi, *Catal. Lett.*, 2020, **150**, 2385–2399.
43 Z. Lin, Y. Lu and J. Huang, *Cellulose*, 2019, **26**, 6683–6700.
44 L. Xu, B. Wei, W. Liu, H. Zhang, C. Su and J. Che, *Nanoscale Res. Lett.*, 2013, **8**, 1–7.
45 T. Tsuru, T. Shutou, S.-I. Nakao and S. Kimura, *Sep. Sci. Technol.*, 1994, **29**, 971–984.
46 Z. Liu, T. Fan, D. Zhang, X. Gong and J. Xu, *Sens. Actuators, B*, 2009, **136**, 499–509.
47 W. Lin, L. Long, L. Yuan, Z. Cao and J. Feng, *Anal. Chim. Acta*, 2009, **634**, 262–266.
48 V. Chau, J. W. Tobias, A. Bachmair, D. Marriott, D. J. Ecker, D. K. Gonda and A. Varshavsky, *Science*, 1989, **243**, 1576–1583.
49 C. Wloka, V. Van Meervelt, D. van Gelder, N. Danda, N. Jager, C. P. Williams and G. Maglia, *ACS Nano*, 2017, **11**, 4387–4394.
50 W. Song, W. Duan, Y. Liu, Z. Ye, Y. Chen, H. Chen, S. Qi, J. Wu, D. Liu and L. Xiao, *Anal. Chem.*, 2017, **89**, 13626–13633.
51 V. D. O. Torres, R. C. Piva, W. F. A. Junior and C. A. L. Cardoso, *Orbital: Electron. J. Chem.*, 2018, **10**, 1–8.
52 V. I. Chalova, I. B. Zabala-Díaz, C. L. Woodward and S. C. Ricke, *World J. Microbiol. Biotechnol.*, 2008, **24**, 353–359.
53 A. Hayat, T. M. Jahangir, M. Y. Khuhawar, M. Alamgir, A. J. Siddiqui and S. G. Musharraf, *J. Cereal Sci.*, 2014, **60**, 356–360.